LAWRENCE
LIVERMORE
NATIONAL
LABORATORY

LLNL-TR-858557

HIGH FIDELITY MODELING OF WELL58-32 DFITS

M. Cusini, F. Fei

December 19, 2023

Disclaimer

This work performed under the auspices of the U.S. Department of Energy by Lawrence Livermore National Laboratory under Contract DE-AC52-07NA27344.

HIGH FIDELITY MODELING OF WELL 58-32 DFITS

Organization:	University of Utah
Recipient Organization:	Lawrence Livermore National Laboratory
DUNS Number:	009095365
Recipient Address:	7000 East Ave. Livermore, CA 94550
Award Number:	2-2446
Project Title:	Closing the loop between in situ stress complexity and EGS fracture complexity
Project Period:	10/01/2021 – 06/30/2025
Principal Investigator(s):	Matteo Cusini (PI) cusini1@llnl.gov Andrew Bunger (Co-PI) bunger@pitt.edu
Report prepared by:	Fan Fei (LLNL) Matteo Cusini (LLNL)
Report Submitted by:	Matteo Cusini
Date of Report Submission:	December 29, 2023
Related milestones:	MILESTONE 1.1.1

This work was performed under the auspices of the U.S. Department of Energy by Lawrence Livermore National Laboratory under Contract DE-AC52-07NA27344.

HIGH-FIDELITY MODELING OF DFITS AT WELL 58-32

1.1 Introduction

Between 2017 and 2019, a series of injection tests were performed at pilot vertical well 58-32 at the Utah FORGE site. These injection activities were conducted in three distinct zones, isolated with packers and bridge plugs during the tests. Zone 1 consists of an open-hole section at the toe of the well, whereas Zones 2 and 3 are three-meter long cased and perforated sections. Several injection cycles were conducted in each zone. A detailed description of the geology of the FORGE site, of well 58-32 and of all injection cycles can be found in (Xing et al., 2020). The injection cycles included Diagnostic Fracture Injection Tests (DFITs). DFITs comprise two primary stages: an injection (pump-in) phase, where controlled fluid injection is employed to create a small hydraulic fracture in the surrounding rock, followed by a shut-in phase, where injection ceases, allowing observation of the formation's pressure response. Utilizing methodologies such as the G-function analysis, DFITs provide valuable insights, including fracture closure pressure and the Instantaneous Shut-in Pressure (ISIP) and can be employed to estimate the minimum horizontal stress (M. W. McClure et al., 2016; M. McClure et al., 2019).

In task 1 of project "Closing the loop between in situ stress complexity and EGS fracture complexity", we aim to employ a high-fidelity geomechanical modeling tool, i.e. the hydraulic fracturing module of the GEOS simulation framework, to model the DFITs conducted at the Utah FORGE site. The primary goals are: (1) to calibrate the numerical model and assess its sensitivity to model parameters to identify reasonable parameters values for the other modeling tasks of the project; (2) to support via numerical modeling the interpretation of the field data that led to the estimation of the minimal horizontal stress. Remark that this work is complementary to the one conducted by other research groups who have employed different modeling tools to model the same field operations. Out of all the injection tests conducted at Well 58-32, a few were DFITs. Here, we focus on the DFIT identified as *Cycle 4* in Zone 2.

We employ a fully-coupled finite element/finite volume approach to solve the coupled solid mechanics and fluid flow equations along with a fracture propagation criterion based on the virtual crack closure technique. Fractures are explicitly modeled using a conforming method. Thus, they are represented by lower dimensional elements (2D in a 3D domain) that sit at the interface of the 3D grid cells as described in (Settgast et al., 2017). To accurately capture the fracture nonlinear closure response after shut-in, we have included the appropriate fracture closure models.

The report is structured as follows: Section 1.2 introduces the governing equations and numerical solution strategy used to model hydraulic fracture growth and closure. Following

that, Section 1.3 presents the modeling approach employed to match the pressure obtained from the FORGE site. Subsequently, parameter sensitivity studies explore the individual impact of modeling parameters on the predicted DFIT response. Lastly, Section 1.4 concludes the report by discussing the obtained results and outlining future plans.

1.2 Formulation and numerical solution strategy

This section summarizes the formulation and the numerical methodology we apply in GEOS hydraulic fracturing solver.

1.2.1 Governing equations

Let us consider a porous domain Ω, with its exterior boundary denoted by $\partial\Omega$. The exterior boundary can be decomposed into two non-overlapping regions subject to Dirichlet and Neumann boundary conditions, respectively. These are identified with $\partial_u\Omega$ and $\partial_t\Omega$ for the solid mechanics equations, $\partial_p\Omega$ and $\partial_q\Omega$ for the fluid flow ones, and they satisfy the following conditions:

$$\partial_u\Omega \cup \partial_t\Omega = \partial\Omega, \quad \partial_u\Omega \cap \partial_t\Omega = \emptyset \tag{1}$$

$$\partial_p\Omega \cup \partial_q\Omega = \partial\Omega, \quad \partial_p\Omega \cap \partial_q\Omega = \emptyset. \tag{2}$$

A single, or a set of fractures Γ, with normal vector n, cut the domain Ω such that the porous matrix is identified by $\mathscr{M} = \Omega \setminus \Gamma$. $\mathscr{M}$ behaves as an elastic permeable medium with a deformation field u, porosity, ϕ, and permeability, k, and it is fully saturated by a single phase fluid with pressure p. Poroelastic effects are solely accounted for by considering a dependency of the matrix porosity on the fluid pressure, i.e.

$$\phi = \phi_0 \left[1 + C_\phi (p - p_0)\right], \tag{3}$$

where p_0 is the reference pressure, ϕ_0 is the reference matrix porosity, and C_ϕ is the pore compressibility. The fluid is considered to be slightly compressible and its density, ρ_f is

$$\rho_f = \rho_0 \left[1 + C_f (p - p_0)\right], \tag{4}$$

where ρ_0 is the reference fluid density and C_f is the fluid compressibility.

Fractures may evolve (propagate) due to the action of the fluid pressure or of an external force. For fluid driven fractures, propagation velocities are generally low and it is appropriate to neglect inertial effects and consider a quasi-static approximation.

Given these preliminaries, the strong form of the initial-boundary-value problem is to find the displacement (u) and pressure (p) fields such that

$$\nabla \cdot \sigma = 0 \quad \text{in } \Omega, \tag{5}$$

$$\frac{\partial}{\partial t}\left(\rho_f \phi\right) + \nabla \cdot \left(\rho_f q_m\right) = q_{ms} \quad \text{in } \Omega \backslash \Gamma, \tag{6}$$

$$\frac{\partial}{\partial t}\left(\rho_f \omega_h\right) + \nabla \cdot \left(\rho_f \omega_h q_f\right) + q_{mf} = q_{fs} \quad \text{in } \Gamma, \tag{7}$$

$$\sigma \cdot n_{\Gamma+} = -\sigma \cdot n_{\Gamma-} = -p n_{\Gamma+} + t_\Gamma \quad \text{on } \Gamma \tag{8}$$

$$\tag{9}$$

subject to

$$u = \hat{u} \quad \text{on } \partial_u \Omega, \tag{10}$$

$$\sigma \cdot v = \hat{t} \quad \text{on } \partial_t \Omega, \tag{11}$$

$$p = \hat{p}_m \quad \text{on } \partial_p \Omega, \tag{12}$$

$$q_m \cdot n_t = \hat{q}_m \quad \text{on } \partial_q \Omega. \tag{13}$$

Here, Eq. (5) is the linear momentum balance and σ is the stress tensor, i.e.

$$\sigma = \mathbb{C} : \nabla^s u, \tag{14}$$

where $\mathbb{C}$ is the fourth-order tensor of mechanical moduli. $\hat{t}$ and $\hat{u}$ denote the prescribed traction and displacement on the exterior boundary, respectively, and n_t is the unit vector normal of $\partial_t \Omega$. Equation (6) describe, instead, the fluid mass balance in the rock matrix. Additionally, q_m is the the fluid velocity in the rock matrix which, according to Darcy's law, reads

$$q_m = -\frac{1}{\mu_f} k \cdot \nabla p_m, \tag{15}$$

where μ_f is the fluid viscosity. q_{ms} are the source/sink term in the rock matrix and $\hat{p}_m$ and $\hat{q}_m$ are the prescribed fluid pressure and fluid velocities.

Equation (7) describes fluid mass balance in the fractures where ω_h is the hydraulic aperture, q_{mf} is the mass flux between the fracture and the porous medium (leak-off) and q_f is the fluid

velocity within the fracture which, according to lubrication theory, can be computed as

$$q_f = -\frac{\omega_h^2}{12\mu_f}\nabla p_f. \tag{16}$$

Finally, Equation (8) is the stress continuity constraint across Γ, where t_Γ is the contact force. Let us ignore, for the sake of simplicity, the tangential components of the force on the fracture surface, such that t_Γ can be expressed by

$$t_\Gamma = -\sigma_{\mathrm{N}} n, \tag{17}$$

where σ_{N} is the magnitude of contact normal stress. In this work, we employ a penalty formulation (Wriggers, 2010) to weakly enforce the non inter-penetration constraint between the two fracture faces, i.e.

$$\sigma_{\mathrm{N}} = \begin{cases} 0 & \text{if } \omega_m > 0, \\ -K_{\mathrm{N}}\omega_m & \text{if } \omega_m \leq 0. \end{cases} \tag{18}$$

Here, K_{N} is the penalty stiffness [1], and $\omega_m := (u_{\Gamma+} - u_{\Gamma-}) \cdot n$ is the normal component of the displacement jump across the fracture (referred to as mechanical aperture).

1.2.2 Fracture propagation criterion

To model fracture propagation induced by fluid injection, we adopt linear elastic fracture mechanics (LEFM) and utilize an enhanced virtual crack closure technique (VCCT) to calculate the stress intensity factor K_I at the crack tip. Once K_I reaches or surpasses the fracture toughness K_{Ic} of the rock, the fracture extends from the tip, creating new crack surfaces by splitting the nodes between adjacent elements. For brevity, the specifics of the enhanced VCCT method are omitted; however, interested readers can find further details in the work by Wu et al. (2021).

1.2.3 Hydraulic aperture model

For perfectly smooth fracture walls, the hydraulic aperture ω_h is always identical to the mechanical aperture ω_m. However, there is broad experimental evidence that fractures in rocks present asperities. As a consequence, there exists a complex nonlinear relationship between contact stresses and the fracture hydromechanical properties (i.e., storativity and permeability).

[1] $K_{\mathrm{N}} = 10^3$ GPa is used throughout this work.

The characterization of the hydraulic aperture-contact stress relationship plays a critical role in accurately capturing the nuances arising from fracture closure during the DFIT shut-in period.

In this work, we consider two distinct, experimentally derived, constitutive relations proposed in the literature. The first relation is derived from the Barton–Bandis model (Barton et al., 1985), reformulated by Willis-Richards et al. (1996) as

$$\omega_h = \frac{\omega_0}{1+9\sigma_{\mathrm{N}}/\sigma_{\mathrm{ref}}}, \tag{19}$$

Here, ω_0 is the hydraulic aperture at zero contact stress, and σ_{ref} is the reference contact stress at which $\omega_h = 0.1\omega_0$.

The second relation is an exponential formulation originating from Li et al. (2021), i.e.

$$\omega_h = \omega_0 \exp\left(-\alpha\sigma_{\mathrm{N}}\right), \tag{20}$$

In the above equation, α is a model parameter characterizing the fracture compressibility.

To facilitate a meaningful comparison between these two models, an equivalent fracture compressibility parameter, denoted as α, can be computed using σ_{ref} to ensure that both models intersect at the reference aperture, which corresponds to 10% of ω_0. Therefore, we can obtain the equivalent fracture compressibility parameter as

$$\alpha = \frac{\ln 10}{\sigma_{\mathrm{ref}}}. \tag{21}$$

An illustrative plot of these two relations is depicted in Fig. 1, considering specific values: $\omega_0 = 12$ mm, $\sigma_{\mathrm{ref}} = 50$ MPa, and an equivalent fracture compressibility $\alpha = 0.046$ MPa^{-1}.

The contact stiffness of the fracture can be computed by evaluating $-\mathrm{d}\sigma_{\mathrm{N}}/\mathrm{d}\omega_h$ (M. McClure et al., 2019). Thus, for the Barton–Bandis model (19), it reads

$$K_{f,\text{Barton˜Bandis}}(\omega_h) = -\frac{\mathrm{d}\sigma_{\mathrm{N}}}{\mathrm{d}\omega_h} = \frac{\sigma_{\mathrm{ref}}}{9}\frac{\omega_0}{\omega_h^2} = \frac{\sigma_{\mathrm{ref}}}{9}\frac{(1+9\sigma_{\mathrm{N}}/\sigma_{\mathrm{ref}})^2}{\omega_0}, \tag{22}$$

whereas, for the exponential model (20) is

$$K_{f,\text{exponential}}(\omega_h) = -\frac{\mathrm{d}\sigma_{\mathrm{N}}}{\mathrm{d}\omega_h} = \frac{\sigma_{\mathrm{ref}}}{\omega_h \ln 10} = \frac{\sigma_{\mathrm{ref}} 10^{\sigma_{\mathrm{N}}/\sigma_{\mathrm{ref}}}}{\omega_0 \ln 10}. \tag{23}$$

In the following section, dedicated to numerical modeling, we conduct a comparative analysis of simulation results obtained using these two models. Our aim is to assess their appropriateness

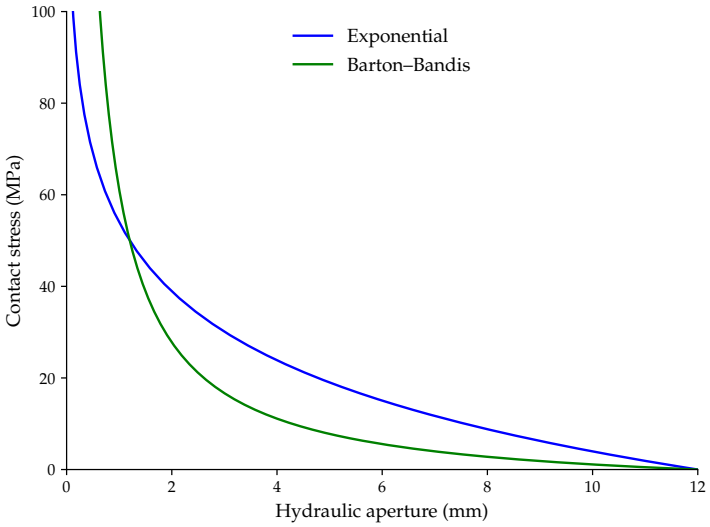

Figure 1: Comparison between two hydraulic aperture models with $\omega_0 = 12$ mm, $\sigma_{\text{ref}} = 50$ MPa, and $\alpha = 0.046$ MPa^{-1}.

to modeling FORGE injection tests. This comparative study will provide insights into the effectiveness and accuracy of each model in capturing the behavior observed during the injection tests conducted at FORGE.

Neither Eq.(19) nor Eq.(20) describe the aperture behavior during the closed state (i.e., $\omega_m \leq 0$). However, during injection and the initial shut-in phase before closure initiates the fracture is open (i.e., $\omega_m > 0$). To address the aperture evolution in the open state, we assume an open fracture between two parallel plates with rough surfaces and a residual aperture, ω_0. This assumption implies that both ω_h and ω_m change in a similar manner when the fracture remains open. Therefore, the complete form of ω_h constitutive relation is

$$\omega_h = \begin{cases} \omega_0 + \omega_m & \text{if } \omega_m > 0, \\ \text{Eq. (19) or Eq. (20)} & \text{if } \omega_m \leq 0. \end{cases} \tag{24}$$

It's important to note that the set of equations presented above can introduce a sharp kink at $\omega_m = 0$, especially when the penalty stiffness is excessively large. This sharp kink may pose numerical challenges for nonlinear convergence.

1.2.4 Discretization and solution strategy

Equations (5), (6), and (7) are discretized, in space, with a low-order finite element discretization of the mechanics equations coupled to a finite volume discretization of the mass balance equations. As for time discretization, an Euler backward method is employed. Thus, at each

time-step, the nonlinear system of discrete equations is solved using a Newton-Raphson method. Once a converged solution is achieved, the propagation criterion is evaluated to determine whether propagation has occurred. Upon fracture propagation, the entire system is re-evaluated for the new fracture configuration until the fracture tip ceases extending. This iterative process allows us to accurately resolve the evolving fracture geometry and associated physical properties until a stable configuration is achieved.

Note that, in the computation of Eq. (16), we utilize ω_h from the previous time step solution to enhance convergence of the Newton-Raphson method.

1.3 Modeling of Zone 2 cycle 4 at well 58-32

In this section, we utilize the formulation, discretization method, and solution strategy detailed in the preceding section 1.2 to simulate the injection test referred to as *Cycle 4* within zone 2 of well 58-32.

The injection rate and the bottom hole pressure (BHP) recorded during the test are presented in Figure 2. Here, the BHP was computed by adding the hydrostatic pressure to the casing pressure reported in GDR submission 1149.

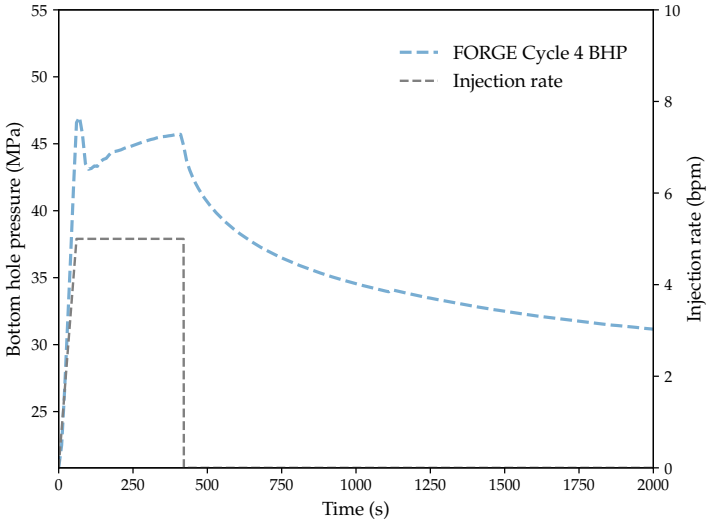

Figure 2: Zone 2 cycle 4 BHP and injection rate data.

1.3.1 Model geometry and boundary conditions

To model the injection test, we consider a cubic homogeneous domain measuring 200 m $\times$ 200 m $\times$ 200 m, depicted in Fig. 3 subjected to in situ stresses. All boundaries of the domain are

constrained by rollers.

Note that, in the field data, the BHP (Fig. 2), after the initial peak indicating breakdown, steadily increases throughout the injection phase. An increasing pressure is typically observed whenever the hydraulic fracture is contained within a layer by a high stress barrier, inducing a pkn-like fracture geometry. However, to the best of our knowledge, there is no evidence of such layering at Utah FORGE. Thus, we assume penny-shaped fracture geometry. The fracture propagates in the direction normal to the minimum horizontal stress, denoted as σ_h. Water injection is considered at the mid point of the initial fracture, employing the injection rate employed during the field test (showed by the grey curve in Fig. 2).

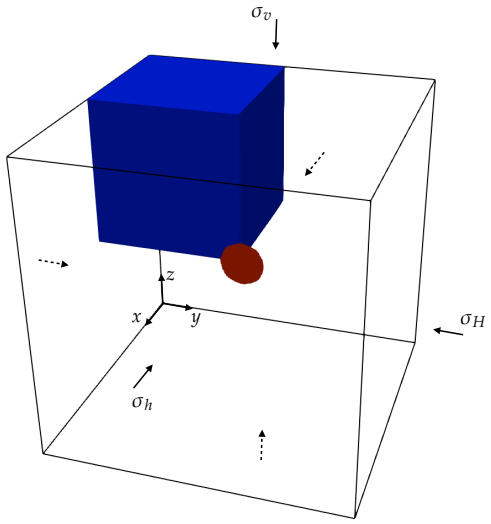

Figure 3: Schematic of the problem domain and boundary conditions.

1.3.2 Solution procedure

To enhance numerical convergence and streamline parameter calibration, the DFIT modeling workflow is divided into two distinct steps, as depicted in Fig. 4. The initial step encompasses simulating fluid injection and fracture propagation until the commencement of shut-in. Subsequently, the modeled hydraulic fracture dimensions and pressure outcomes are processed and transferred to a separate model. This separate model is designed specifically to simulate fluid leak-off and fracture closure during the shut-in period, where the hydraulic fracture ceases propagation.

Consistency is maintained across both steps by utilizing identical material parameters, in situ stresses, and hydrostatic pressure conditions. This consistency ensures a coherent and accurate representation of the hydraulic fracture's behavior throughout the simulation process.

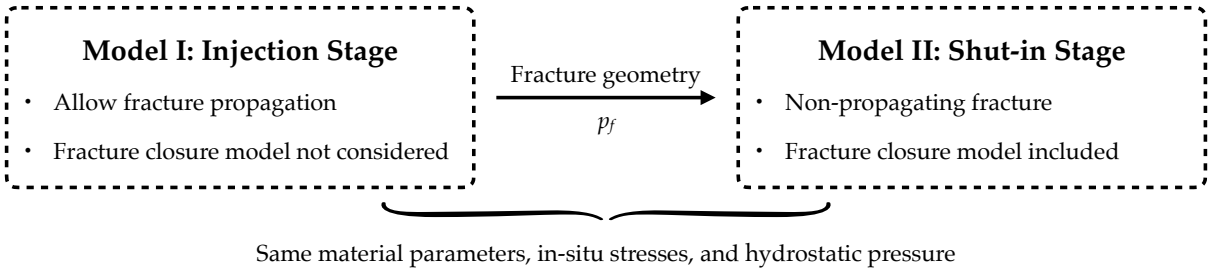

Figure 4: Workflow employed for DFIT modeling that separately solves the injection and shut-in stages.

1.3.3 Model calibration

The in situ stress values, and the rock and fluid properties considered in the model are presented in Tables 1 and 2, respectively. Initial values for the simulation parameters are adopted from Xing et al. (2021). The matrix permeability k, the minimum horizontal stress, the hydraulic aperture model and its parameters (*i.e.,* ω_0, σ_{ref}, and α) have been calibrated to reproduce the field-data BHP curve. Simulations employing the exponential hydraulic aperture law seem to better reproduce the field data.

Minimum horizontal stress, σ_h	44.5 MPa
Maximum horizontal stress, σ_H	50.7 MPa
Vertical stress, σ_v	65.2 MPa
Hydrostatic pressure, p_0	20.8 MPa

Table 1: Initial conditions applied in the simulation.

Elastic modulus, E	GPa	50
Poisson's ratio, ν	-	0.25
Fracture toughness, K_{Ic}	MPa·m$^{1/2}$	1.75
Matrix permeability, k	m^2	8×10^{-16}
Porosity, ϕ	-	0.01
Pore compressibility, C_ϕ	MPa^{-1}	1.9×10^{-3}
Fluid viscosity, μ_f	cp	1
Fluid compressibility, C_f	MPa^{-1}	5×10^{-4}
Initial aperture, ω_0	mm	12
Reference contact stress, σ_{ref}	MPa	50
Equivalent fracture compressibility, α	MPa^{-1}	0.046

Table 2: Rock and fluid properties adopted in the simulation.

GEOS simulation results obtained with the calibrated parameters are presented in Fig. 5. As demonstrated in Fig. 5a, with the calibrated parameters, the simulation results have a decent

agreement with field data for breakdown pressure, shut-in pressure, and the pressure decay trend during the shut-in period. Following the modeled fracture pressure data, we construct the G-function plot showcased in Fig. 5b. As expected, analysis of the G-function plot (Economides & Nolte, 1989; M. W. McClure et al., 2016) indicates that the fracture initiates closure when the bottom hole pressure decreases to approximately 44.5 MPa, aligning precisely with the minimum horizontal stress applied within the model.

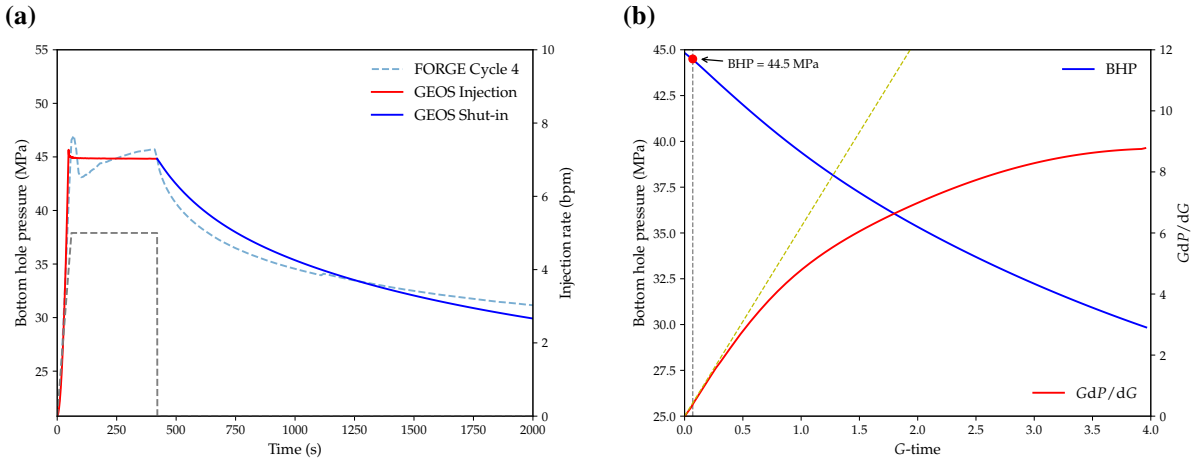

Figure 5: GEOS simulation of the Cycle 4 test in Zone 2 of Well 58-32 using the exponential model (20): (a) comparison of BHP curve obtained with GEOS against the field data from Utah FORGE; (b) G-function plot.

In the next subsections we investigate the sensitivity of the results to the hydraulic aperture model and to some of the model parameters.

1.3.4 Effect of the hydraulic aperture model

Here, we investigate how the simulation outcomes are influenced by the choice of the hydraulic aperture model. Thus, we conduct a new shut-in simulation utilizing the Barton–Bandis model while maintaining all other input parameters constant. Fig. 6a shows a comparison of the results obtained with the two aperture models. Note, that the pressure curve generated by the Barton–Bandis model exhibits a slightly concave trend, which contrasts with the generally convex shapes observed in both the curves obtained using the exponential model and observed in the field measurement data. This distinction highlights the differences between the two fracture closure models. The discrepancy can be explained by analyzing the ω_h-σ_N relation in Fig. 6. It's apparent that during the initial stages of fracture closure ($\omega_h \approx \omega_0$), the Barton–Bandis model demonstrates a slower increase in the contact stress, leading to a more gradual

pressure reduction compared to the exponential model. However, as the fracture stiffness (*i.e.*, $-\mathrm{d}\sigma_\mathrm{N}/\mathrm{d}\omega_h$) increases at a much swifter rate within the Barton–Bandis model (see Eqs. (22) and (23)), significant closure of the fracture ($\omega_h \ll \omega_0$) triggers a notably accelerated rise in the contact stress, subsequently resulting in a faster decline in pressure.

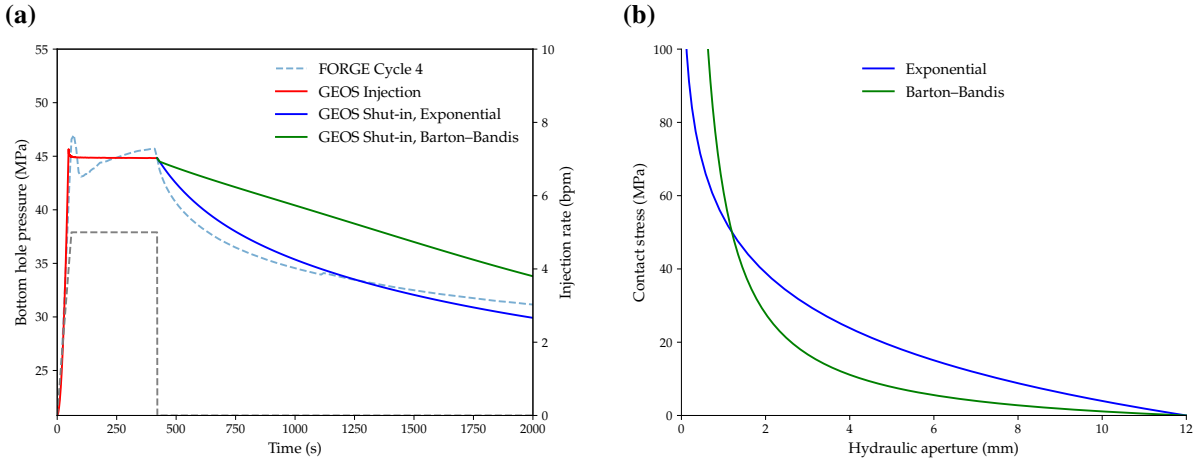

Figure 6: Comparison between two fracture closure models: (a) simulation results of the Cycle 4 test in Well 58-32; (b) ω_h-σ_N relations.

1.3.5 Sensitivity to model parameters

We now explore the sensitivity of the model to the initial aperture ω_0 and of the reference contact stress σ_ref, with their respective outcomes presented in Fig. 7 and 8.

As shown in Fig. 7a, a reduction in ω_0 results in a faster pressure decay. This acceleration can be attributed to the higher fracture stiffness observed in the scenario with a smaller initial aperture (see Eq. (23)), as illustrated in Fig. 7b. Consequently, a faster increase in contact stress occurs when ω_h decreases (indicating fracture closure), which results in a faster pressure reduction.

A similar rationale applies when analyzing the effect of σ_ref: Fig. 8b demonstrates that a larger σ_ref corresponds to a higher fracture stiffness (see Eq. (23)). This correlation leads to a more rapid pressure decline during shut-in, as observed in Fig. 8a.

Finally, we investigate the sensitivity of the results to the fracture toughness and the matrix permeability. Fig. 9a compares the results with different values of fracture toughness. As expected, a higher K_{Ic} results in a higher breakdown pressure. The matrix permeability, has little influence on the pressure curve during the injection phase (see Fig. 9b), likely because the

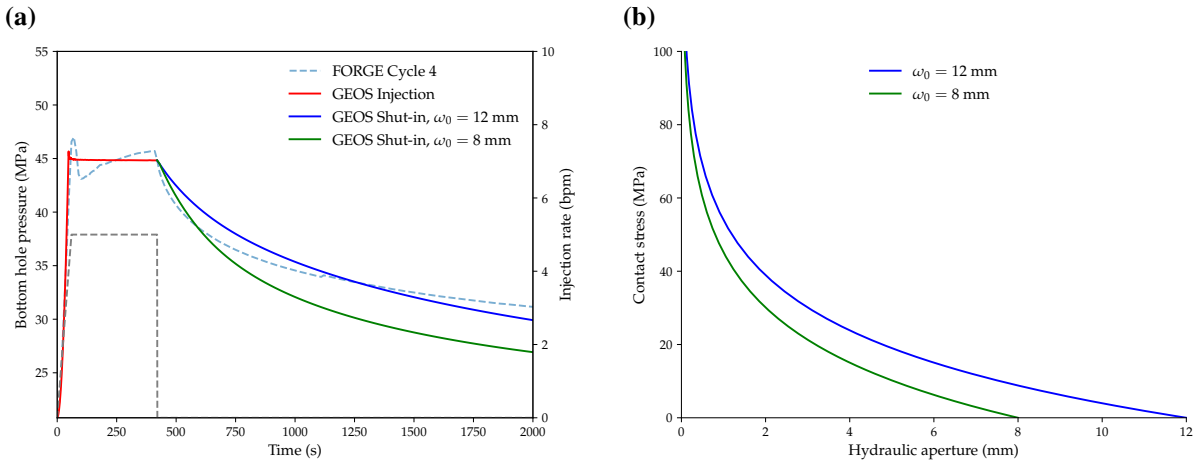

Figure 7: Comparison between two cases with different ω_0: (a) simulation results of the Cycle 4 test in Well 58-32; (b) ω_h-σ_N relations.

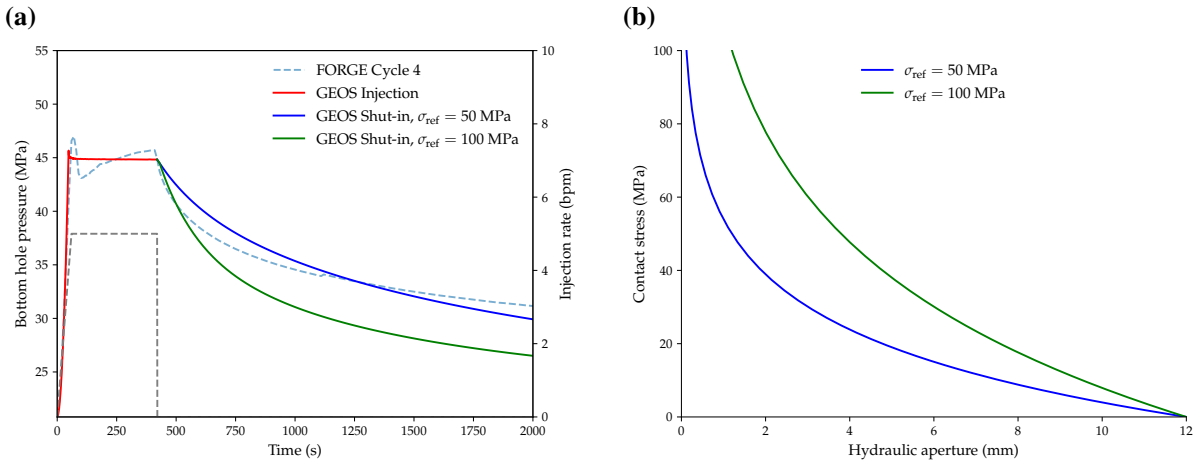

Figure 8: Comparison between two cases with different σ_{ref}: (a) simulation results of the Cycle 4 test in Well 58-32; (b) ω_h-σ_N relations.

process is in a storage-dominated regime. However, a substantial impact is observed after shut-in; as expected, a lower matrix permeability leads to a significantly slower pressure reduction. In fact, a low matrix permeability slows down the fluid leak-off during fracture closure, thereby delaying the pressure drop.

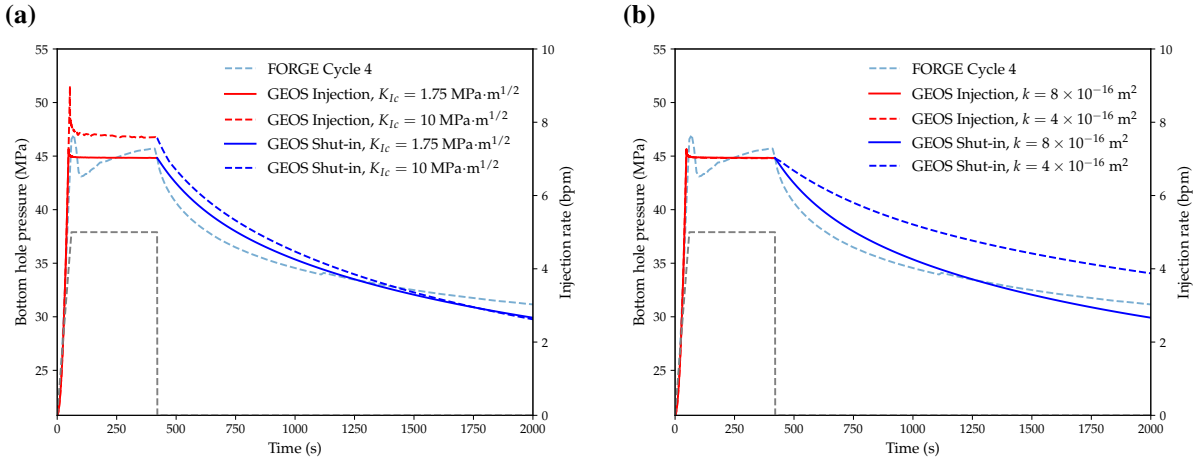

Figure 9: Comparison between simulation results with different (a) fracture toughness K_{Ic} and (b) permeability k.

1.4 Conclusions and future work

To summarize, in this report, we have presented our effort to model one of the DFITs conducted at FORGE well 58-32 using GEOS hydraulic fracturing module. Some key points deserve to be highlighted:

- The inferred minimum horizontal stress from our numerical study (44.5 MPa) closely aligns with reported values (ranging from 41.7 to 44.9 MPa) by Xing et al. (2020). These values were derived from diverse techniques used to analyze Zone 2 injection test results.
- The exponential model (20) seems to better reproduce the field data compared to the Barton–Bandis model (19).
- All outcomes from parameter sensitivity studies align with theoretical expectations and can be theoretically justified, consolidating their credibility.
- While the initial aperture used ($\omega_0 = 12$ mm) might appear relatively large compared to experimental measurements (commonly in the magnitude of 10^{-1} mm according to

sources like (Li et al., 2021; Meng et al., 2022), it's essential to consider potential scaling effects. The substantial difference in fracture size between our simulation (approximately 20 m) and laboratory scales (approximately 100 mm) suggests a potential scaling effect on hydraulic aperture, which could validate the chosen ω_0 value. Further research accounting for this scaling effect is recommended to substantiate the choice of ω_0 in our simulation.

The remaining discrepancies between the simulation outcomes and field observations highlight areas for further investigation. Specifically, notable discrepancies include the gradual increase observed in the field-data BHP curve post-breakdown. As highlighted in (Xing et al., 2020) potential mechanisms that may explain such a pressure curve are: (i) poroelastic effects and (ii) the interaction between the hydraulic fracture and the natural fracture network. Future and ongoing research efforts will focus on employing the numerical model to explore how these effects may affect the BHP curve and thus have an impact on interpretation techniques. Moreover, we are currently investigating the the impact thermal effects may have.

MODEL AVAILABILITY

All results showcased in this report were generated utilizing GEOS, an open-source subsurface simulator. The GEOS codebase along with all input files used to run the models presented can be accessed and downloaded from its official website at www.geos.dev.

REFERENCES

Barton, N., Bandis, S., & Bakhtar, K. (1985). Strength, deformation and conductivity coupling of rock joints. In *International journal of rock mechanics and mining sciences & geomechanics abstracts* (Vol. 22, pp. 121–140).

Economides, M. J., & Nolte, K. G. (1989). *Reservoir stimulation* (Vol. 2). Prentice Hall Englewood Cliffs, NJ.

Li, W., Frash, L. P., Welch, N. J., Carey, J. W., Meng, M., & Wigand, M. (2021). Stress-dependent fracture permeability measurements and implications for shale gas production. *Fuel*, *290*, 119984.

McClure, M., Bammidi, V., Cipolla, C., Cramer, D., Martin, L., Savitski, A., ... Voller, K. (2019, 07). *A Collaborative Study on DFIT Interpretation: Integrating Modeling, Field Data, and Analytical Techniques* (Vols. Day 2 Tue, July 23, 2019). Retrieved from https://doi.org/10.15530/urtec-2019-123 doi: 10.15530/urtec-2019-123

McClure, M. W., Jung, H., Cramer, D. D., & Sharma, M. M. (2016). The fracture-compliance method for picking closure pressure from diagnostic fracture-injection tests. *Spe Journal*, *21*(04), 1321–1339.

Meng, M., Frash, L. P., Li, W., Welch, N. J., Carey, J. W., Morris, J., ... Kneafsey, T. (2022). Hydro-mechanical measurements of sheared crystalline rock fractures with applications for egs collab experiments 1 and 2. *Journal of Geophysical Research: Solid Earth*, *127*(2), e2021JB023000.

Settgast, R. R., Fu, P., Walsh, S. D., White, J. A., Annavarapu, C., & Ryerson, F. J. (2017). A fully coupled method for massively parallel simulation of hydraulically driven fractures in 3-dimensions. *International Journal for Numerical and Analytical Methods in Geomechanics*, *41*(5), 627–653.

Willis-Richards, J., Watanabe, K., & Takahashi, H. (1996). Progress toward a stochastic rock mechanics model of engineered geothermal systems. *Journal of geophysical research: solid earth*, *101*(B8), 17481–17496.

Wriggers, P. (2010). *Computational contact mechanics*. Heidelberg: Springer Berlin. doi: https://doi.org/10.1007/978-3-540-32609-0

Wu, H., Settgast, R. R., Fu, P., & Morris, J. P. (2021). An enhanced virtual crack closure technique for stress intensity factor calculation along arbitrary crack fronts and the application in hydraulic fracturing simulation. *Rock Mechanics and Rock Engineering*, *54*, 2943–2957.

Xing, P., Damjanac, B., Radakovic-Guzina, Z., Finnila, A., Podgorney, R., Moore, J., & McLennan, J. (2021). Numerical simulation of injection tests at utah forge site. In *Proceedings of the 46th workshop on geothermal reservoir engineering, stanford university, stanford, ca, usa, february 16* (Vol. 18).

Xing, P., McLennan, J., & Moore, J. (2020). In-situ stress measurements at the utah frontier observatory for research in geothermal energy (forge) site. *Energies*, *13*(21), 5842.